

## Inelastic photoproduction of $\omega$ and $\rho^\pm$ mesons

C. A. Nelson, Jr., E. N. May, J. Abramson,\* D. E. Andrews,<sup>†</sup> J. Harvey, F. Lobkowicz, M. N. Singer,<sup>‡</sup> and E. H. Thorndike

*Department of Physics and Astronomy, University of Rochester, Rochester, New York 14627*

M. E. Nordberg, Jr.

*Laboratory of Nuclear Studies, Cornell University, Ithaca, New York 14850*

(Received 22 October 1976)

We report measurements of inelastic photoproduction of  $\omega$  and  $\rho^\pm$  mesons from hydrogen and deuterium at incident photon energies in the range 7.5–10.5 GeV. For  $\omega\Delta$  and  $\rho^-\Delta^{++}$  production, differential cross sections  $d\sigma/dt'$  and spin density matrices are presented. For higher missing masses the cross sections  $d\sigma/dM_x^2$  and invariant structure functions  $F(x)$  are also given. The data are compared to a one-pion-exchange model. We conclude that pion exchange is dominant for inelastic  $\omega$  photoproduction, but unimportant for  $\rho^\pm$ .

### I. INTRODUCTION

We have measured photoproduction of  $\omega$  and  $\rho^\pm$  mesons from protons and deuterons in the 7.5–10.5 GeV energy range. The data were taken at the Cornell 12-GeV electron synchrotron using a tagged photon beam and a forward particle spectrometer. In addition to elastic production, we observe substantial cross sections for production of  $\Delta(1236)$  as well as a continuum of higher masses, in which no resonant structure is resolved, extending up to missing masses squared of 10 GeV<sup>2</sup>, the limit of our detection sensitivity. Results on elastic  $\omega$  and  $\rho^\pm$  photoproduction have already been presented.<sup>1,2</sup> In this paper we present data on the reactions

$$\gamma N \rightarrow \omega \Delta(1236), \quad (1a)$$

$$\gamma p \rightarrow \rho^-\Delta^{++}(1236), \quad (1b)$$

$$\gamma N \rightarrow \omega X(2.2 < M_x^2 < 10 \text{ GeV}^2), \quad (1c)$$

$$\gamma N \rightarrow \rho^\pm X(2.5 < M_x^2 < 10 \text{ GeV}^2). \quad (1d)$$

The  $\omega$  reactions are expected to be dominated by pion exchange.  $\rho$  exchange is expected to dominate the  $\rho^\pm$  reactions, but there may be substantial contributions from  $\pi$  and  $A_2$  exchanges as well.

In contrast to the situation for elastic  $\rho^0$  and  $\omega$  photoproduction, little experimental work has been reported for the reactions listed above. An upper limit of 0.5  $\mu\text{b}$  has been reported<sup>3</sup> for  $\gamma n \rightarrow \omega\Delta^0$  ( $\Delta^0 \rightarrow p\pi^-$ ) at 4.3 GeV incident photon energy. Previous experiments<sup>3,5</sup> of  $\gamma p \rightarrow \rho^-\Delta^{++}$  conflict in their findings. The data of Refs. 3 and 4 show cross sections falling from  $\sim 2$  to  $\sim 1$   $\mu\text{b}$  in the energy range 3 to 8 GeV, but streamer-chamber measurements<sup>5</sup> at DESY claim lower values, about 0.5  $\mu\text{b}$ , in the range 3 to 6 GeV. For the meson decay angular distributions, which provide fur-

ther information on the exchange mechanisms, results have been reported for  $\gamma p \rightarrow \rho^-\Delta^{++}$  only.

For  $\omega\Delta$  and  $\rho^\pm\Delta$  production we present the differential cross sections  $d\sigma/dt'$ , where  $t' \equiv |t - t_{\min}|$ , and the meson spin density matrices evaluated in the Gottfried-Jackson (GJ) frame. The cross sections are compared to a one-pion-exchange (OPE) calculation given by Wolf.<sup>6</sup> For the more highly inelastic regions, we present differential cross sections  $d\sigma/dt'$  and  $d\sigma/dM_x^2$ , where  $M_x$  is the mass of the system recoiling from the  $\omega(\rho^\pm)$ , and the invariant structure function

$$F(x) \equiv \frac{1}{\pi} \int \frac{E^*}{P_{\max}^*} \frac{d^2\sigma}{dx dp_\perp^2} dp_\perp^2, \quad (2)$$

where  $x$  is defined as  $p_{\parallel}^*/(p_{\max}^{*2} - p_\perp^2)^{1/2}$ , the ratio of the meson longitudinal momentum in the overall center-of-mass system to its maximum allowed value at the same  $p_\perp^2$ . The range of integration is 0 to 0.4 GeV<sup>2</sup>. The  $\omega$  and  $\rho^\pm$  spin density matrices are given for the GJ frame. For missing masses squared less than 4.5 GeV<sup>2</sup>, differential cross sections are compared to an OPE model, which we formulated by extending a conventional OPE model to apply to inclusive reactions. Finally, the  $\rho^+ - \rho^-$  charge asymmetry from deuterium is given as a function of  $M_x^2$ .

The organization of the paper is as follows: Apparatus and experimental procedures are discussed in Sec. II. In Sec. III data analysis is discussed and results are presented. Conclusions are summarized in Sec. IV. The OPE calculations are outlined in the Appendix.

### II. EXPERIMENTAL

The experimental apparatus is shown in Fig. 1. Bremsstrahlung photons from an 11.25-GeV electron beam were tagged in the energy range 8.8

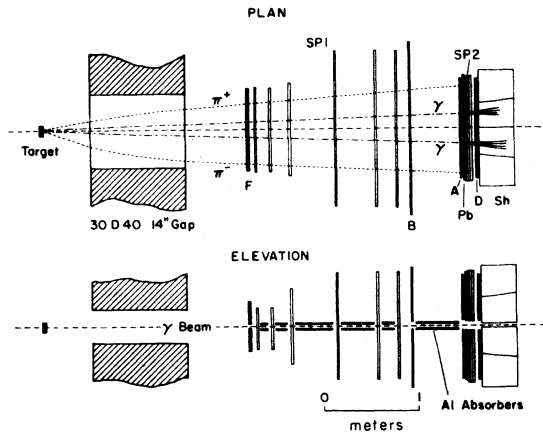


FIG. 1. Plan and elevation view of the detector.

to 10.4 GeV (Ref. 7) by a 16-bin hodoscope consisting of 17 overlapping counters. After collimation and charged-particle removal, the photon beam passed through a liquid hydrogen or deuterium target, located just upstream of a 30D40 magnet.  $\omega$  and  $\rho^\pm$  mesons were detected through their dominant decay modes:  $\omega \rightarrow \pi^+\pi^-\pi^0$ ,  $\rho^\pm \rightarrow \pi^\pm\pi^0$ ,  $\pi^0 \rightarrow \gamma\gamma$ . Charged pions exiting from the magnet passed through a front plane of four scintillation counters (F), six wire spark chambers (SP1) and a back plane of four counters (B). The spark chambers were deadened in the median plane so that the photon beam and  $e$  pairs produced in the target would not pass through their sensitive region. Lead and aluminum absorbers protected the active chamber regions against soft particles produced as the beam passed through the array. The two-track spark-chamber efficiency was 98% at low beam intensity, and 94% at the operating intensity ( $\sim 10^6$  tagged photons/sec, average rate).

The  $\gamma$  detector measured both positions and energies of the  $\pi^0$ -decay  $\gamma$  rays. After passing through the charged-pion detector and a  $4 \times 4$  array of anticoincidence counters (A), the  $\gamma$  rays entered a 1.5-radiation-length Pb converter. Three strip spark chambers measured the shower positions with a two-track efficiency of 97% at operating intensity. Following the spark chambers were a  $4 \times 4$  array of scintillation counters (D) and a  $4 \times 4$  array of Čerenkov shower counters (S). To allow the beam and the associated "sheet" of  $e$  pairs to pass through, the  $\gamma$  detector was divided into two parts by a 2-inch gap in the median plane. Each of the two Čerenkov-counter halves consisted of a stainless-steel tank filled with an aqueous solution of lead perchlorate and subdivided by thin light baffles into eight nearly identical sections. Each section was viewed by four 5-in. photomultipliers, whose outputs were added, integrated,

and digitized. The rms percentage energy resolution of the  $\gamma$  detector was  $17\%/[E(\text{GeV})]^{1/2}$ .

The shower-counter calibrations were obtained by three independent methods: (1) sweeping electrons of known energy into the counters, (2) putting a tagged photon beam of the appropriate energy range into the counters, and (3) requiring that the reconstructed  $\pi^0$  mass be correct, independent of  $\pi^0$  energy and independent of the S-counter pairings struck by the two photons. Agreement among the three methods was good.

The trigger condition for  $\omega$  events was

$$(\text{tagged photon}) \cdot (\bar{>2F} \text{ counters}) \\ \cdot (\bar{>2B} \text{ counters}) \cdot (\bar{>2\gamma}),$$

where  $\gamma$  was defined by  $\bar{A} \cdot D \cdot S$  for any one of the 16 sections. For  $\rho^\pm$  events the requirement was

$$(\text{tag}) \cdot (\bar{>1F}) \cdot (\bar{>1B}) \cdot (\bar{>2\gamma}) \cdot (E_s),$$

where the  $E_s$  condition meant that at least 3.5 GeV had been deposited in the shower counters. This last condition was necessary to hold the  $\rho^\pm$  trigger rate to acceptable levels. An on-line PDP-11 computer wrote the events onto magnetic tape, displayed events on a storage scope, performed diagnostic checks, and passed the data to a PDP-10 computer for track finding and kinematic reconstruction. Data recorded for each event included spark-chamber information, digitized pulse areas for each S counter, latch information for the tag, F, B, and  $\gamma$  counters, and times of arrival for the tag, F, and D counter signals. Between beam bursts, the on-line computer checked photomultiplier stabilities by monitoring their response to pulses from light emitting diodes mounted on the counters.

Since the momenta of all the vector-meson decay products were measured and the incident photon energy was known, the missing mass recoiling against the vector meson was determined. The energy resolution of the Čerenkov shower counters contributed most to the resolution in missing mass squared, which was typically  $0.3 \text{ GeV}^2$  rms for  $\omega$  events and  $0.5 \text{ GeV}^2$  rms for  $\rho^\pm$ .

### III. DATA ANALYSIS AND RESULTS

Events were reconstructed assuming that the production point was at the center of the target. Charged particles were assumed to be pions. The required topology was two charged tracks plus  $2\gamma$  for  $\omega$  events and one charged track plus  $2\gamma$  for  $\rho^\pm$ . Figure 2 shows a  $\gamma\gamma$  mass spectrum for events satisfying the  $\omega$  topology. The full width at half maximum (FWHM) of the  $\pi^0$  peak agrees well with the expected width of 35 MeV. For events passing a  $\pi^0$  mass cut the  $\gamma\gamma$  mass was

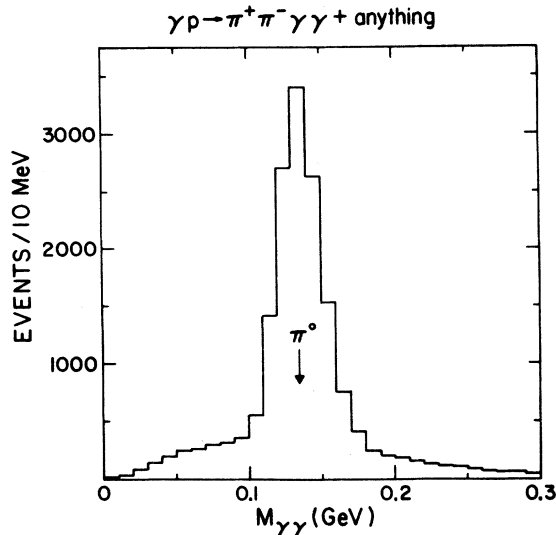


FIG. 2.  $\gamma\gamma$  mass spectrum for events satisfying the  $\omega$  topology requirement.

then forced to the value  $m_{\pi^0}$  by adjusting the  $\gamma$ -ray energies by amounts proportional to their uncertainties. At equal photon energies, this amounted to using the opening angle to determine the  $\pi^0$  energy. This procedure substantially improved the  $\pi^0$  energy resolution and consequently the resolutions in reconstructed meson mass and missing mass.

All final distributions have been corrected for contamination due to randoms falling inside the timing cuts and for nonresonant background underneath the  $\omega$  ( $\rho^\pm$ ) mass peak. Corrections for random coincidences are based on time difference distributions for each  $M_X^2$  and  $t'$  bin. These corrections, typically less than 10%, are found to be independent of  $t'$  but increasing with  $M_X^2$ . Nonresonant backgrounds inside the  $\omega$  mass cut are substantial (ranging from 17% for  $2.2 < M_X^2 < 4.5$  GeV<sup>2</sup> to 58% for  $7 < M_X^2 < 10$  GeV<sup>2</sup>) but easily estimated since the  $\omega$  peak is sharp (FWHM = 35 MeV) and the background nearly flat. The  $\rho^\pm$  peak, however, sits atop a large, rapidly falling background. It was necessary to fit the observed  $m_{\pi\pi}$  spectrum, for each  $t'$ ,  $M_X^2$ , and  $x$  bin, to a  $\rho$  shape plus a smooth background.

Detector acceptances were determined by Monte Carlo calculations, using the meson decay angular distributions as measured in this experiment. In quoting accuracies for our overall cross-section normalizations, we allow for contributions from uncertainties in the decay distributions.

Except for the production of  $\rho\Delta(1236)$ , we have used hydrogen and deuterium data together to determine cross sections per nucleon:

$$\text{cross section/nucleon} = [\sigma(\gamma p) + \frac{1}{2}\sigma(\gamma d)]/1.88, \quad (3)$$

where we divide by 1.88, not 2, to allow for a Glauber correction factor of 0.88 for the deuterium cross sections. Spin density matrices are straight averages. In all cases for which the combining was done, the hydrogen and deuterium results were identical to within the experimental uncertainties. Fermi motion within the deuteron worsens the  $M_X^2$  resolution at the largest  $M_X^2$  points;  $M_X^2$  resolution at low  $M_X^2$  and  $t'$  resolution are not significantly worsened.

#### $\omega$ production

The  $\omega$  data were collected in two separate runs. The first (tagging range 7.3 to 8.9 GeV) had the better  $M_X^2$  resolution ( $\sigma = 0.25$  GeV<sup>2</sup>) but poorer detection efficiency, particularly for larger missing masses. The second (tagging range 8.8 to 10.4 GeV) had larger acceptance, but poorer  $M_X^2$  resolution ( $\sigma = 0.32$  GeV<sup>2</sup>). For  $M_X^2$  less than 4.5 GeV<sup>2</sup>, the cross sections  $d\sigma/dt'$  and spin density matrices as obtained separately for the two runs were in good agreement, and were therefore combined to yield the final results. Other results are as obtained from the second run.

Figure 3 shows the  $M_X^2$  spectra for  $\gamma p \rightarrow \omega X$  as obtained in the two runs. For both spectra the elastic peak is noticeably broadened by the presence of a  $\Delta(1236)$  signal, which appears as a shoulder in the first spectrum but is unresolved in the second. To extract the  $\Delta$  signal it was necessary to use an unfolding procedure based on the expected  $M_X^2$  shapes for elastic,  $\Delta(1236)$ , and non- $\Delta$  inelastic final states. For the non- $\Delta$  inelastic final states we developed an OPE model for inclusive reactions. A brief description of this model is given in the Appendix. The expected  $\Delta$  distribution was obtained from an OPE calculation smeared by experimental resolution, and the shape of the elastic spectrum was simply the resolution function. In Figs. 3(a) and 3(b) the dashed curves show the relative amounts of elastic,  $\Delta(1236)$ , and non- $\Delta$  inelastic (OPE) as obtained by fitting the expected shapes to the observed distributions.

The unfolding procedure used was as follows: Three  $M_X^2$  regions were defined I. 0.4 to 1.2 GeV<sup>2</sup> (dominated by the elastic final state), II. 1.3 to 1.8 GeV<sup>2</sup> [a mixture of elastic,  $\Delta(1236)$ , and non- $\Delta$  inelastic events], and III. 2.2 to 4.5 GeV<sup>2</sup> (mostly non- $\Delta$  inelastic events). For each region, the number of events in each  $t'$  bin, corrected for random and non- $\omega$  background, was obtained from the data. From Monte Carlo studies, the fraction of elastic,  $\Delta(1236)$ , and non- $\Delta$  inelastic events

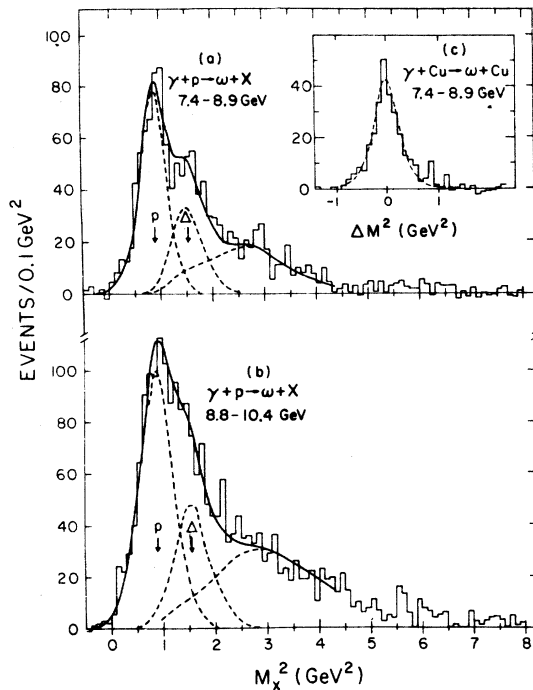


FIG. 3. Missing-mass-squared distribution for  $\omega$  photoproduction: from hydrogen as obtained from (a) the first, and (b) the second data collection runs; and (c) from copper, as obtained from the first run, after isolation of the coherently produced signal. The solid lines in (a) and (b) are fits to the expected shapes for elastic,  $\Delta(1236)$  and non- $\Delta$  inelastic production, as shown by the dashed curves. Fit range was 0 to 4.5  $\text{GeV}^2$ . In (c)  $\Delta M^2$  is the reconstructed missing-mass squared minus the value expected for coherent production. The dashed curve in (c) shows the expected shape.

falling into each mass region was determined. The nine fractions together with the number of events in each region form a set of three simultaneous linear equations with three unknowns, the unknowns being the number of elastic,  $\Delta(1236)$ , and non- $\Delta$  inelastic events for the  $t'$  bin.

The reliability of the unfolding procedure depends on the accuracy with which the Monte Carlo simulation reproduces the missing-mass resolution. We have obtained a direct measurement of this resolution by studying  $\omega$  photoproduction from copper, under experimental conditions identical to those of Fig. 3(a). By accepting only events for which  $t' < 0.02 \text{ GeV}^2$ , we obtained a data sample for which coherent production is the dominant mechanism. The small incoherent signal in this  $t'$  region was eliminated by subtracting an appropriately scaled missing-mass-squared ( $\text{MM}^2$ ) spectrum of events at larger values of  $t'$ , beyond the coherent region. The signal thus obtained is

virtually purely elastic, and thus directly measures the missing-mass resolution and calibrates the missing-mass scale. The resulting  $\text{MM}^2$  distribution is shown in Fig. 3(c), along with the distribution predicted by the Monte Carlo calculation. Agreement is excellent. By fitting these data to Monte Carlo distributions with various widths and central positions, it was determined that the data are best described by an  $M_x^2$  resolution function with a width of  $0.99 \pm 0.09$  times the expected value, and that a shift of  $0.02 \text{ GeV}^2$  in the  $M_x^2$  scale is allowed. Less direct measures (e.g., the  $\pi^0$  mass distribution) confirm the correctness of the Monte Carlo resolution at a level better than 10%. Taking  $1.0 \pm 0.1$  as the correction factor for the resolution, we repeated the unfolding procedure with resolution functions broader (and narrower) by 10%. From this we determined that the  $\pm 10\%$  uncertainty in resolution caused a  $\pm 2.5\%$  error in the elastic absolute cross section, and even smaller errors in the  $\Delta$  and non- $\Delta$  inelastic cross sections. Elastic and non- $\Delta$  inelastic  $t'$  distributions are unchanged, while the  $\Delta t'$  distribution is changed by about  $\frac{1}{3}$  of the statistical errors. The  $\Delta$  cross section varies by only  $\pm 1\%$  when the  $M_x^2$  scale is allowed to shift by  $\pm 0.02 \text{ GeV}^2$ , and by  $\pm 2\%$  if the  $M_x^2$  scale shift and resolution are allowed to vary simultaneously. The elastic and non- $\Delta$  inelastic cross sections are not significantly affected by a shift in the  $M_x^2$  scale. In short, uncertainties in the missing-mass resolution and scale introduce negligible errors into the unfolding procedure.

The reliability of the unfolding procedure depends mainly on the accuracy with which the OPE reproduces the non- $\Delta$  inelastic spectrum, particularly in the region of the  $\Delta$ . For the region  $2.2 \leq M_x^2 \leq 4.5 \text{ GeV}^2$  the model reproduces the  $M_x^2$  distributions shown in Fig. 3, and (as will be shown) adequately describes the shape and magnitude of the differential cross section  $d\sigma/dt'$ . One is thus inclined to believe that the OPE model will not be far off at lower missing masses.<sup>8</sup> To investigate the sensitivity of elastic and  $\Delta$  results, we modified the OPE cross section by multiplying by a factor which was 1.0 for  $M_x^2 \geq 2.2$ , and rose linearly to 2.0 as  $M_x^2$  dropped to threshold. With this characterization of the non- $\Delta$  inelastic spectrum, the unfolding procedure gave an elastic cross section that was lower by 2%, and a  $\Delta$  cross section lower by 15%. The  $\Delta t'$  distribution became steeper, though well within statistical errors. We (somewhat arbitrarily) assume that the model modification just described is a 1.5-standard-deviation effect, and take  $\pm 10\%$  as the systematic uncertainty in the  $\Delta$  cross section due to the unfolding procedure.

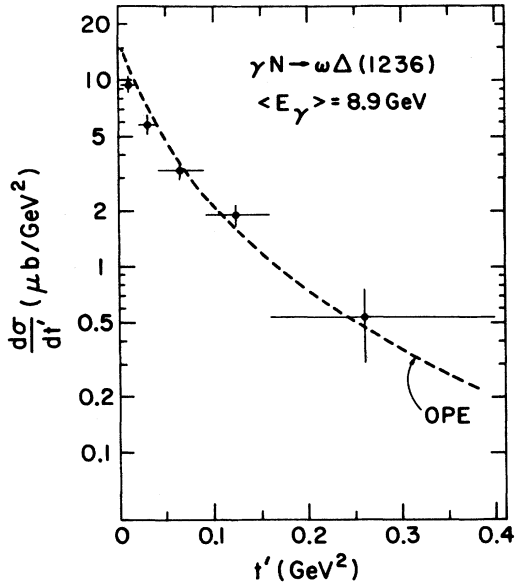


FIG. 4. Differential cross section  $d\sigma/dt'$  for the reaction  $\gamma N \rightarrow \omega\Delta(1236)$  at an effective energy of 8.9 GeV. The curve is from an OPE calculation discussed in the text.

The differential cross section for  $\gamma N \rightarrow \omega\Delta$  is shown in Fig. 4. In addition to the errors shown, there is a  $\pm 15\%$  normalization uncertainty, which includes the  $\pm 10\%$  systematic uncertainty in the

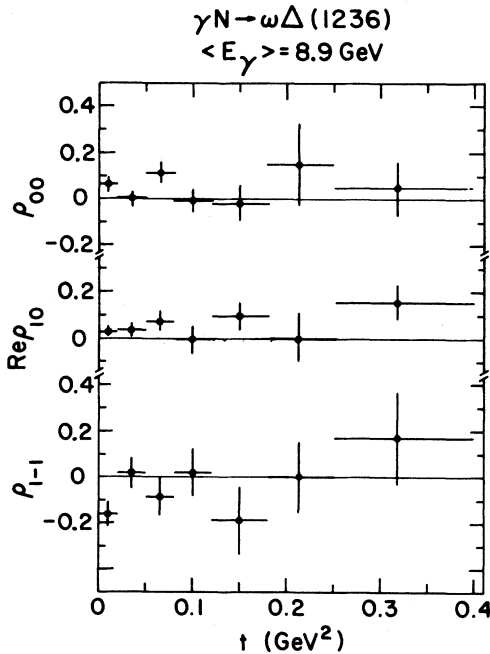


FIG. 5. Spin density matrix, evaluated in the Gottfried-Jackson frame, for the reaction  $\gamma N \rightarrow \omega\Delta(1236)$  at 8.9 GeV.

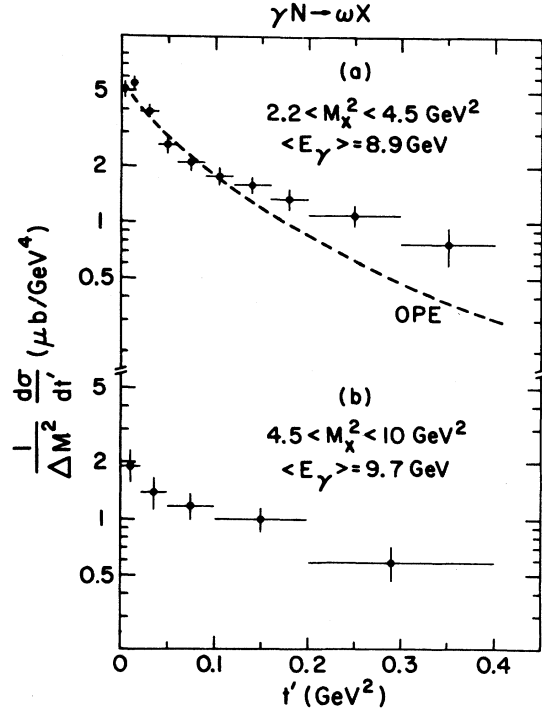


FIG. 6. Differential cross sections  $d\sigma/dt'$  for the reaction  $\gamma N \rightarrow \omega X$ : (a)  $2.2 < M_X^2 < 4.5 \text{ GeV}^2$  at 8.9 GeV and (b)  $4.5 < M_X^2 < 10 \text{ GeV}^2$  at 9.7 GeV. The cross sections have been divided by the respective missing-mass-squared intervals. The curve in (a) is from an inclusive OPE model discussed in the text.

unfolding procedure. The curve is from an OPE calculation, the formalism for which is described in the Appendix. The strength of the  $\gamma\pi\omega$  coupling has been determined from the  $\omega \rightarrow \pi^0\gamma$  radiative decay width, taken to be 0.9 MeV. The strength of the  $N\pi\Delta$  vertex is obtained from the cross section for  $\pi N \rightarrow \Delta$ . Other parameters are taken from Wolf.<sup>6</sup> The model therefore is a zero-free-parameter description of the reaction  $\gamma N \rightarrow \omega\Delta$ . It describes the  $t'$  distribution well, and although 15% too high in absolute magnitude, is within the normalization uncertainty.

The spin density matrix for  $\gamma N \rightarrow \omega\Delta$ , evaluated in the GJ frame, is shown in Fig. 5. The results approximate  $t$ -channel helicity conservation ( $\rho_{00} = \text{Re}\rho_{10} = \rho_{1-1} = 0$ ) as expected for simple OPE. Thus the reaction  $\gamma N \rightarrow \omega\Delta$  is described correctly by OPE in both the differential cross section and spin density matrix.

Differential cross sections for the mass regions above the  $\Delta$  are shown in Fig. 6. Overall normalization is uncertain to  $\pm 15\%$ . The conventional OPE calculation using coupling constants cannot be applied to this mass region because of the many overlapping resonances, and because of substan-

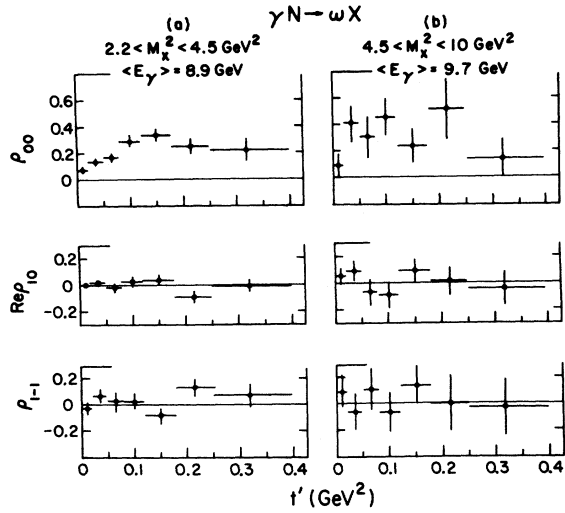


FIG. 7. Spin density matrices for the reaction  $\gamma N \rightarrow \omega X$ : (a)  $2.2 < M_X^2 < 4.5 \text{ GeV}^2$  at  $8.9 \text{ GeV}$ , (b)  $4.5 < M_X^2 < 10 \text{ GeV}^2$  at  $9.7 \text{ GeV}$ .

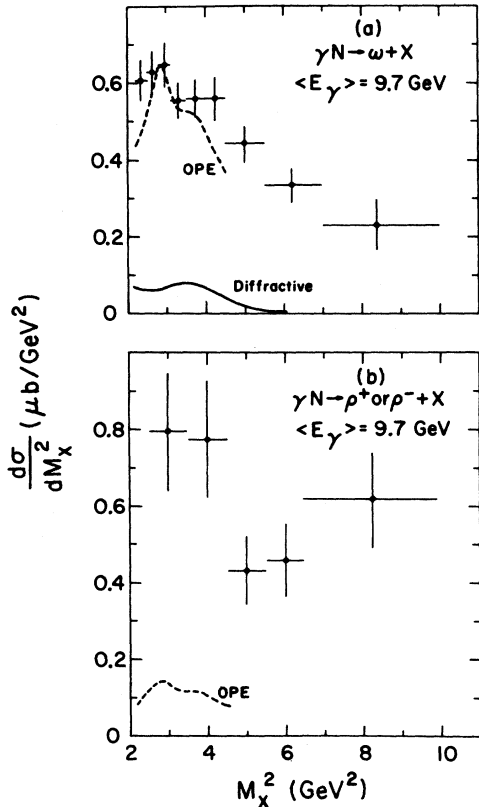


FIG. 8. Differential cross sections  $d\sigma/dM_X^2$  for (a)  $\gamma N \rightarrow \omega X$  and (b)  $\gamma N \rightarrow \rho^\pm X$  at  $9.7 \text{ GeV}$ . Data shown are for  $t' < 0.4 \text{ GeV}^2$ . Dashed curves are expected OPE contributions. The solid curve in (a) shows the estimated contribution from diffractive inelastic production.

tial nonresonant production. We have therefore extended the OPE model to describe inclusive reactions. In doing this we describe the  $\pi N \rightarrow X$  vertex by  $\pi N$  phase shifts at  $s = M_X^2$  as elaborated upon in the Appendix. In Fig. 6(a) the data are compared to our OPE model. The agreement is remarkable for  $t' < 0.1 \text{ GeV}^2$ , but the curve is consistently low for  $t' > 0.1 \text{ GeV}^2$ . No OPE curve is shown for Fig. 6(b), due to the unavailability of the  $\pi N$  phase shifts over this mass range.

Spin density matrix elements for the two higher missing-mass intervals are displayed against  $t'$  in Fig. 7. The data are consistent with the helicity conservation in the forward direction, but by  $t' = 0.1 \text{ GeV}^2$ ,  $\rho_{00}$  has risen to a value consistent with isotropic decay ( $\rho_{00} = \frac{1}{3}$ ,  $\text{Re} \rho_{10} = \rho_{1-1} = 0$ ). The rise appears somewhat steeper for the higher missing-mass region. It is interesting to note that, even at small  $t'$ , the spin density matrix deviates significantly from the simple OPE expectation of  $t$ -channel helicity conservation in spite of the good agreement between OPE and the

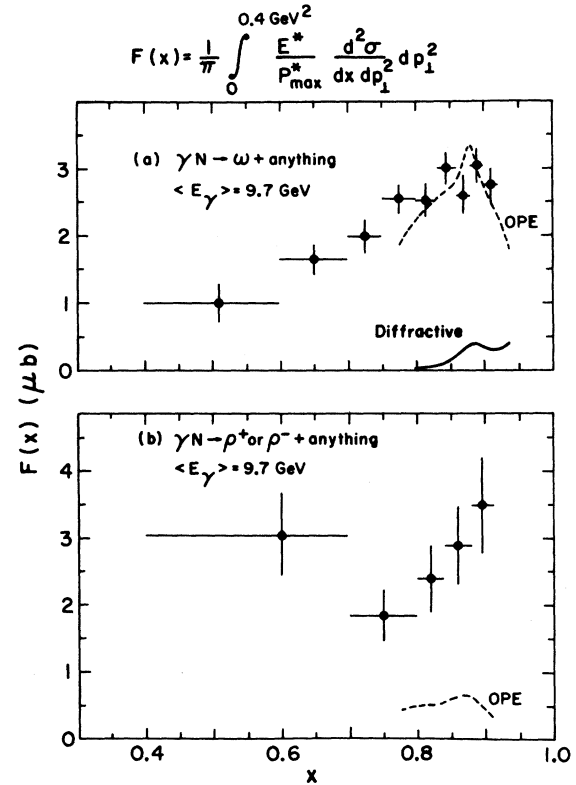


FIG. 9. Invariant structure functions for (a)  $\gamma N \rightarrow \omega X$  and (b)  $\gamma N \rightarrow \rho^\pm X$  at  $9.7 \text{ GeV}$ . The range of  $p_{\perp}^2$  integration is  $0$  to  $0.4 \text{ GeV}^2$ . The dashed curves are expected OPE contributions. The solid curve in (a) shows the estimated contribution from diffractive inelastic production.

data in Fig. 6(a).

The differential cross section  $d\sigma/dM_x^2$  and the invariant structure function  $F(x)$  are shown in Figs. 8(a) and 9(a). The data show a rise in  $F(x)$  in the  $x$  interval 0.4 to 0.9. Inclusive  $\rho^0$  photoproduction, by comparison, has been found<sup>9</sup> to give  $F(x) \approx 1.3 \mu\text{b}$ , nearly independent of  $x$  in the interval 0 to 0.8. The OPE model describes the data reasonably well but appears to fall off too rapidly as inelasticity increases.

Inelastic  $\omega$  photoproduction via diffractive mechanisms is expected to be small. The solid lines in Figs. 8(a) and 9(a) show our estimate of inelastic diffractive production, based on calculations presented by Wolf.<sup>10</sup>

#### $\rho^\pm$ production

The  $m_{\pi^+\pi^0}$  distribution for  $M_x^2$  less than  $2.5 \text{ GeV}^2$  is shown in Fig. 10. It contains a prominent  $\rho^\pm$  peak which we extracted by assuming the background to be linear in the  $\rho$  region. The  $M_x^2$  distribution obtained in this way for the reaction  $\gamma p \rightarrow \rho^- X^{++}$  is displayed in Fig. 11. For  $M_x^2$  less than  $2.5 \text{ GeV}^2$  the observed distribution is consistent with being entirely due to production of  $\rho^- \Delta^{++}(1236)$ .

In Fig. 12 we display the cross section  $d\sigma/dt'$  for  $\gamma p \rightarrow \rho^- \Delta^{++}$ . The errors shown allow for the uncertainties in extracting the  $\rho^\pm$  signal from the nonresonant backgrounds, but do not include an overall normalization uncertainty of  $\pm 15\%$ . The solid curve is the contribution expected from OPE.

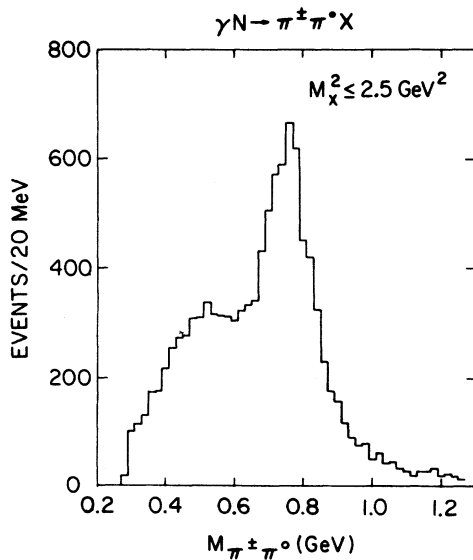


FIG. 10.  $\pi^+\pi^0$  mass distribution for events satisfying the  $\rho^\pm$  topology and having a missing mass squared less than  $2.5 \text{ GeV}^2$ .

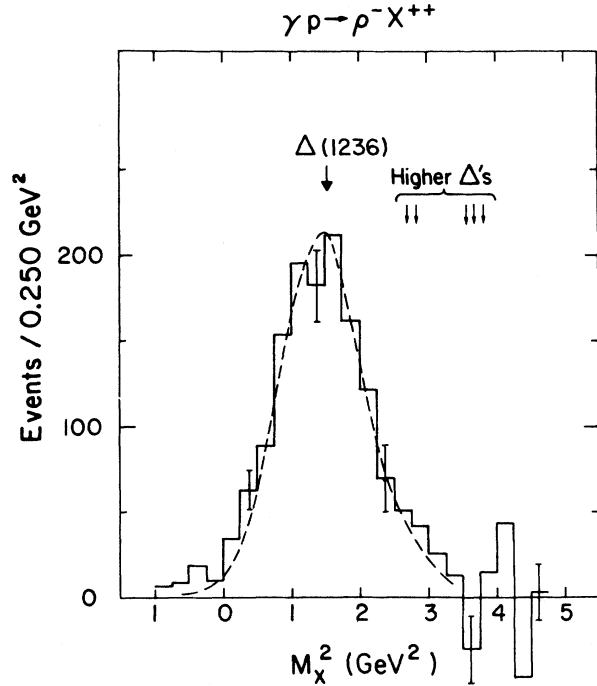


FIG. 11. Missing-mass-squared distribution for  $\rho^-$  production from hydrogen. The curve shows the distribution expected for  $\rho^- \Delta^{++}(1236)$ . Note that the distribution is not reliable above  $M_x^2 = 2.5 \text{ GeV}^2$  because the background-subtraction procedure used to obtain this distribution is appropriate for  $M_x^2 < 2.5 \text{ GeV}^2$  only.

In contrast to the reaction  $\gamma N \rightarrow \omega \Delta$ ,  $\rho^- \Delta^{++}$  production is not well reproduced by OPE. The sharp forward peaking of the OPE calculation<sup>11</sup> is not present in the data and the total OPE cross section is only 21% of the observed cross section in the

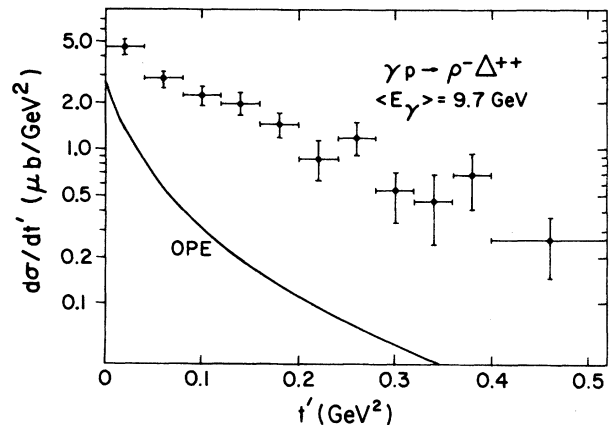


FIG. 12. Differential cross section  $d\sigma/dt'$  for the reaction  $\gamma p \rightarrow \rho^- \Delta^{++}(1236)$  at  $9.7 \text{ GeV}$ . The curve shows the expected OPE contribution.

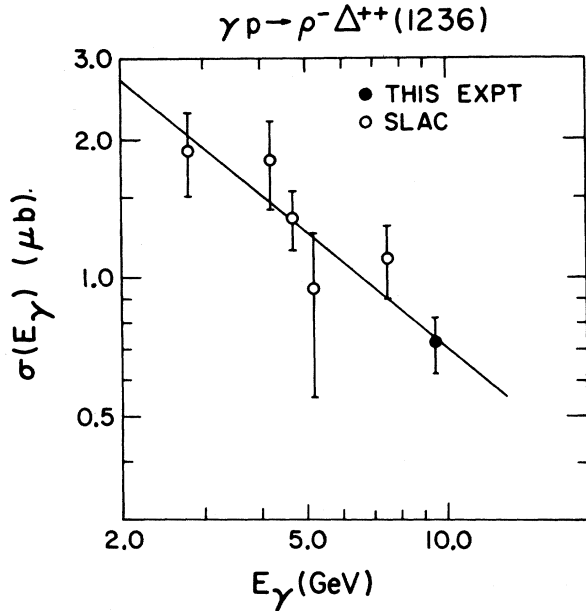


FIG. 13. Energy dependence of the reaction  $\gamma p \rightarrow \rho^- \Delta^{++}(1236)$ . The line is a fit to the form  $C E_\gamma^{-n}$ , as discussed in the text. The points labeled SLAC are from Refs. 3 and 4.

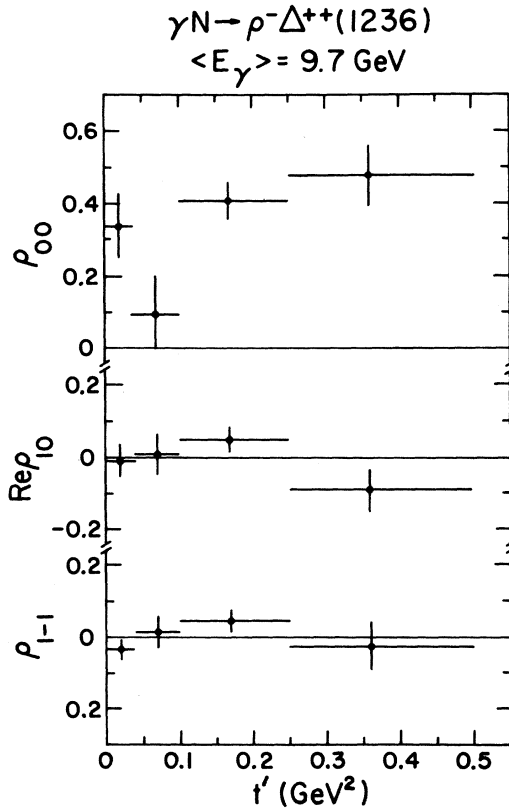


FIG. 14. Spin density matrix for the reaction  $\gamma p \rightarrow \rho^- \Delta^{++}(1236)$  at 9.7 GeV, as evaluated in the Gottfried-Jackson frame.

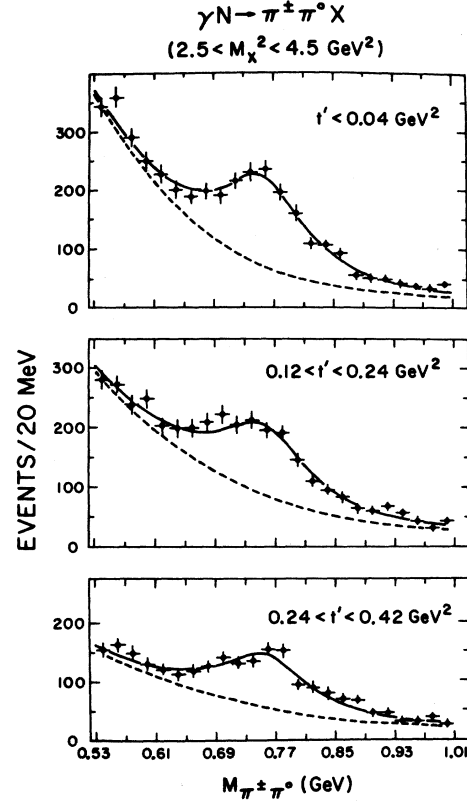


FIG. 15.  $\pi^+ \pi^0$  mass distributions for  $\gamma N \rightarrow \pi^+ \pi^0 X$ , for  $2.5 < M_X^2 < 4.5 \text{ GeV}^2$ . Distributions are shown for these  $t'$  regions. The solid curves are fits to a  $\rho$  shape plus background (dashed curves), as discussed in the text.

$t'$  interval 0 to 0.2  $\text{GeV}^2$ . Fitting the data to the form  $d\sigma/dt' = A e^{-bt'}$  we find  $A = 4.9 \pm 0.3 \text{ } \mu\text{b}/\text{GeV}^2$  and  $b = 7.2 \pm 1 \text{ GeV}^{-2}$ , consistent with slopes reported for a previous experiment.<sup>4</sup>

The energy dependence for  $\gamma p \rightarrow \rho^- \Delta^{++}$ , obtained from this and earlier experiments,<sup>3,4</sup> is displayed in Fig. 13. The curve is a fit to the form  $C E_\gamma^{-n}$ , with  $C = 4.7 \pm 0.4 \text{ } \mu\text{b}$  and  $n = 0.81 \pm 0.18$ . Reactions dominated by pion exchange have larger  $n$  values in the range 1.6–2.5. On the other hand, this energy dependence is reasonable for  $\rho$ - $A_2$  exchange.

In Fig. 14 we show the spin density matrix for  $\gamma p \rightarrow \rho^- \Delta^{++}$ , evaluated in the GJ frame. Deviation from  $t$ -channel helicity conservation is large. The data more nearly approximate an isotropic decay distribution ( $\rho_{00} = \frac{1}{3}$ ,  $\text{Re} \rho_{10} = \rho_{1-1} = 0$ ).

For missing masses above the  $\Delta(1236)$ , a simple straight-line characterization of the background is inadequate. Figure 15 shows the  $\pi^+ \pi^0$  mass distributions for various  $t'$  bins in the  $M_X^2$  interval 2.5 to 4.5  $\text{GeV}^2$ . The solid lines are fits to the

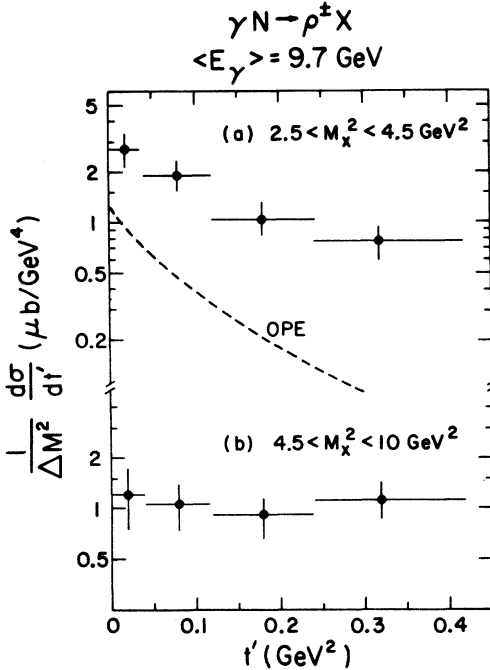


FIG. 16. Differential cross sections  $d\sigma/dt'$ , for the reaction  $\gamma N \rightarrow \rho^\pm X$ : (a)  $2.5 < M_X^2 < 4.5 \text{ GeV}^2$ , and (b)  $4.5 < M_X^2 < 10 \text{ GeV}^2$ . The cross sections have been divided by the respective missing mass squared intervals. The curve in (a) is from an inclusive OPE model discussed in the text.

form

$$N(m_{\pi\pi}) = [A_\rho f_\rho(m_{\pi\pi}) + f_B(m_{\pi\pi})] \times \text{Acceptance}(m_{\pi\pi}), \quad (4)$$

where the  $\rho$  shape  $f_\rho$  is a relativistic  $p$ -wave Breit-Wigner of fixed mass ( $m_0 = 0.77 \text{ GeV}$ ) and width ( $\Gamma_0 = 0.15 \text{ GeV}$ ), and the background term  $f_B$  is of the form

$$f_B(m_{\pi\pi}) = A_B \{1 + \alpha [\Delta m + \beta(t') \Delta m^2]\}, \quad \Delta M = m_{\pi\pi} - m_0. \quad (5)$$

The extracted  $\rho^\pm$  signal  $A_\rho$  is particularly sensitive to the amount of background curvature, i.e., the parameter  $\beta$ . Therefore  $\beta$  was constrained to vary smoothly from one binning interval to the next. The procedure was as follows: In the initial fits,  $A_\rho$ ,  $A_B$ ,  $\alpha$ , and  $\beta$  were all allowed to vary. The fitted  $\beta$  values were then plotted against the binning variable, e.g.,  $t'$ , and a smooth characterization  $\beta(t')$  and uncertainty  $\delta\beta$  were chosen. This  $\beta(t')$  was then used in the final fits to determine  $A_\rho$ ,  $A_B$ , and  $\alpha$  for each  $t'$  bin.

The resulting differential cross sections are shown in Fig. 16.  $\rho^+$  and  $\rho^-$  cross sections have been summed. As was the case for  $\omega$  production, the slope for the higher missing-mass interval is

significantly smaller than for the lower interval. The expected contribution from pion exchange, shown by the curve, is again a small part of the observed cross section.

Figure 17 shows the spin density matrices. Data for  $\rho^+$  and  $\rho^-$  have been averaged. The data in the lower missing-mass interval approximate an isotropic decay distribution, but for the higher mass interval  $\rho_{00}$  is large, about 0.7, at  $t' < 0.1 \text{ GeV}^2$ , and  $\text{Re}\rho_{10}$  and  $\rho_{1-1}$  depart slightly from zero for  $t' > 0.1 \text{ GeV}^2$ . This behavior does not conform to any simple expectation.

The cross section  $d\sigma/dM_X^2$  and the invariant structure function  $F(x)$  are shown together with the same quantities for  $\omega$  production, in Figs. 8(b) and 9(b). Cross sections for  $\rho^+$  and  $\rho^-$  have again been summed. In the  $x$  interval 0.4 to 0.7, the  $\rho^\pm$  inclusive cross section is substantially larger than that of the  $\omega$ , but from  $x = 0.7$  to 0.9 they appear similar.

Finally, from the deuterium data, we have obtained the  $\rho^+ - \rho^-$  charge asymmetry:

$$\epsilon_d(M_X) \equiv \frac{\sigma(\gamma d \rightarrow \rho^+ M_X) - \sigma(\gamma d \rightarrow \rho^- M_X)}{\sigma(\gamma d \rightarrow \rho^+ M_X) + \sigma(\gamma d \rightarrow \rho^- M_X)}. \quad (6)$$

$\epsilon_d(M_X)$  is plotted in Fig. 18. (We have integrated over the  $t'$  range 0.0 to  $0.4 \text{ GeV}^2$ .) A nonzero value of the charge asymmetry implies interference between trajectories of opposite  $G$  parity. The

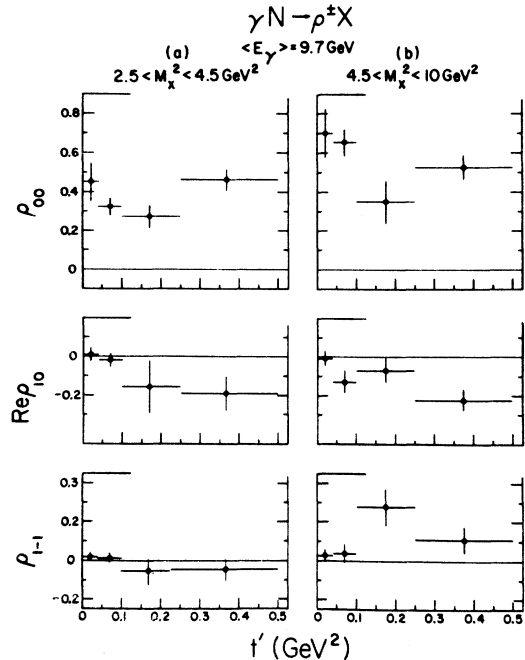


FIG. 17. Spin density matrices for  $\gamma N \rightarrow \rho^\pm X$ : (a)  $2.5 < M_X^2 < 4.5 \text{ GeV}^2$ , and (b)  $4.5 < M_X^2 < 10 \text{ GeV}^2$ .

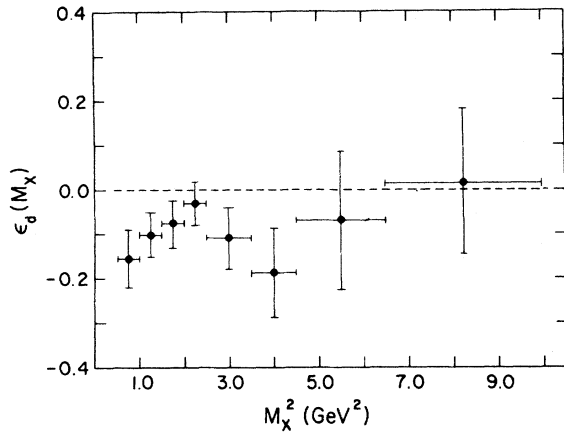


FIG. 18. Charge asymmetry for  $\rho^\pm$  photoproduction from deuterium as a function of  $M_x^2$ .

asymmetry is observed to be near zero everywhere, but the departure from zero at low  $M_x^2$  is significant. This has been interpreted<sup>2</sup> in terms of  $\rho$ - $A_2$  exchange-degeneracy breaking.

#### IV. SUMMARY

From our measurements of  $\omega$  and  $\rho^\pm$  inelastic photoproduction we conclude the following:

- (1) Photoproduction of  $\omega\Delta(1236)$  is consistent with a pion exchange mechanism. The  $t$  dependence and absolute magnitude of the cross section are well reproduced by an OPE calculation. The decay angular distribution is approximately consistent with  $t$ -channel helicity conservation as expected in a simple OPE picture.
- (2) The cross section for  $\gamma N \rightarrow \omega X$ ,  $2.2 < M_x^2 < 4.5$ , is well described by an OPE model for  $t' < 0.1$  GeV<sup>2</sup>, but the spin density matrix shows significant departure from  $t$ -channel helicity conservation. For  $0.1 < t' < 0.4$  GeV<sup>2</sup> the OPE calculation is about 66% of the observed cross section and the spin density matrix is consistent with isotropic decay. If OPE is indeed the dominant production mechanism, then the simple OPE picture must be modified, e.g., by absorption, to account for the observed decay angular distribution.
- (3) As expected, inelastic  $\rho^\pm$  photoproduction is not consistent with pion exchange for any reaction studied. In particular, for the reaction  $\gamma p \rightarrow \rho^+ \Delta^{++}$ , the  $t$  dependence, energy dependence and absolute magnitude of the cross section, and the spin density matrix, indicate that pion exchange plays at most a minor role.

#### ACKNOWLEDGMENTS

We wish to thank the operations staff of the Wilson Synchrotron Laboratory at Cornell University

for the smooth operating conditions during these experiments. The authors gratefully acknowledge the interest and support of Professor B. D. McDaniel, and thank him for his hospitality during their stay at Cornell. This research was supported by the National Science Foundation.

#### APPENDIX

Here we briefly discuss the OPE model for vector-meson photoproduction. We first describe the calculation for  $\gamma N \rightarrow V\Delta(1236)$  and then describe our extension of the formulas to the reaction  $\gamma N \rightarrow V + \text{anything}$ .

##### A. $\gamma N \rightarrow V\Delta(1236)$

Following Wolf,<sup>6</sup> we write the OPE differential cross section for the diagram in Fig. 19(a) as follows:

$$\frac{d^2\sigma}{d|t|dM_\Delta} = \frac{1}{4\pi^3 p^{*2} s} |T_{V\gamma\gamma}|^2 \frac{1}{(t - \mu^2)^2} |T_{N\gamma\Delta}|^2, \quad (\text{A1})$$

where  $s$  is the square of the center-of-mass (c.m.) energy,  $\rho^*$  is the c.m. momentum of the photon,  $t$  is the square of the four-momentum transfer, and  $\mu$  is the pion mass.

The  $V\pi\gamma$  vertex function is proportional to the vector-meson radiative width,  $\Gamma_{V\gamma\gamma}$ :

$$|T_{V\gamma\gamma}|^2 = 3\pi^2 \frac{\Gamma_{V\gamma\gamma}}{k^3} m_V^2 q^2 \frac{u_1(q_t R_V)}{u_1(q R_V)}, \quad (\text{A2})$$

where  $k$  is the energy of the decay photon in the vector-meson rest frame,  $q$  is the pion momentum for an on-mass-shell pion, and  $q_t$  is the virtual pion momentum. Correction for the off-mass-shell nature of the pion is performed by the term  $u_1(q_t R_V)/u_1(q R_V)$ . The functions of  $u_1(x)$ , discussed in more detail in Ref. 6, have the behavior  $u_1 \sim x^{2l}$  at small  $x$  ( $x \ll 1$ ) so that the ratio

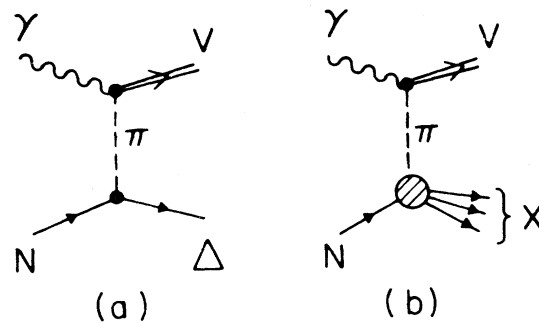


FIG. 19. OPE diagrams for inclusive vector-meson photoproduction: (a)  $\gamma N \rightarrow V\Delta(1236)$  and (b)  $\gamma N \rightarrow V + \text{anything}$ .

$$\frac{u_1(q_t R)}{u_1(q R)} \approx \left(\frac{q_t}{q}\right)^2,$$

yields a correction appropriate for the Born approximation. For  $x \gg 1$ ,  $u_1(x)$  falls as  $x^{-2} \ln(4x^2)$ . Thus the parameter  $R_\gamma$  assumes the role of a cut-off radius. Following Ref. 6, we use  $R_\omega = R_\rho = 0.46$  F.

The nucleon vertex term  $|T_{N\Delta}|^2$  is given by

$$|T_{N\Delta}(t, M)|^2 = M^2 Q C_{p33}(t, M) \sigma_{\pi N}^{p33}(s = M^2). \quad (\text{A3})$$

$M$  is the  $\pi N$  mass,  $Q$  is the momentum of a real pion in the  $\Delta$  rest frame,  $\sigma_{\pi N}^{p33}$  is the  $\pi N$  cross section in the  $p33$  channel, and the  $C_{p33}$  term is given by

$$C_{p33} = \frac{(M + m_N)^2 - t}{(M + m_N)^2 - \mu^2} \frac{u_1(Q_t R_{p33})}{u_1(Q R_{p33})}, \quad (\text{A4})$$

where  $Q_t$  is the momentum of the virtual pion in the  $\Delta$  rest frame, and  $R_{p33}$  is taken to be 0.35 F, as given by Ref. 6.

#### B. $\gamma N \rightarrow V + \text{anything}$

In the above calculation, the nucleon vertex is characterized by a single cross section,  $\sigma_{\pi N \rightarrow \Delta}$ . To describe the inclusive process diagrammed in Fig. 19(b) the nucleon vertex must include contributions from many resonances and nonresonant

final states as well. We therefore write the nucleon vertex term in Eq. (A1) as a sum of  $\pi N$  partial cross sections, each multiplied by an appropriate correction term:

$$|T_{N\pi X}(t, M)|^2 = M^2 Q \sum_{L, J, I} C_{L, J, I}(t, M) \sigma_{\pi N}^{L, J, I}(s = M^2). \quad (\text{A5})$$

In our calculations, the sum extends to orbital angular momentum  $L = 4$ , with total angular momentum  $J = L \pm \frac{1}{2}$  and isospin  $I = \frac{1}{2}, \frac{3}{2}$ . The  $C$  factors again contain the ratio  $u_L(Q_t R_{L, J, I})/u_L(Q R_{L, J, I})$ . The  $R$  parameters, taken from Ref. 6, are typically 0.3 to 0.9 F. In order to have a complete set of these cutoff radii, we had to assume them to be independent of isospin. A complete description of the factors  $C_{L, J, I}$  and a discussion of the  $R$  parameters is given in Ref. 6.

The partial cross sections  $\sigma_{\pi N}^{L, J, I}$  were obtained from a  $\pi N$  phase shift analysis<sup>12</sup>:

$$\sigma_{\pi N}^{L, J, I} = \frac{4\pi}{Q} \text{Im}[f_{\pi N}^{L, J, I}(\theta = 0)], \quad (\text{A6})$$

where  $f_{\pi N}^{L, J, I}$  is the  $\pi N$  elastic scattering amplitude, at  $s = M^2$ , in the  $L, J, I$  partial wave. The  $M^2$  range of this model is currently limited to 4.7 GeV<sup>2</sup> and below, due to the absence of  $\pi N$  phase-shift information above  $s = 4.7$  GeV<sup>2</sup>.

\*Present address: Department of Radiation Biology and Biophysics, University of Rochester, Rochester, New York 14642.

†Present address: Laboratory of Nuclear Studies, Cornell University, Ithaca, New York 14853.

‡Present address: Southeastern Massachusetts University, New Bedford, Massachusetts 02747.

<sup>1</sup>J. Abramson *et al.*, Phys. Rev. Lett. **36**, 1428 (1976).

<sup>2</sup>J. Abramson *et al.*, Phys. Rev. Lett. **36**, 1432 (1976).

<sup>3</sup>Y. Eisenberg *et al.*, Phys. Rev. Lett. **25**, 764 (1970).

<sup>4</sup>J. Ballam *et al.*, Phys. Rev. Lett. **26**, 995 (1971);

Y. Eisenberg *et al.*, Phys. Rev. D **5**, 15 (1972).

<sup>5</sup>W. Struczinski *et al.*, Nucl. Phys. **B108**, 45 (1976).

<sup>6</sup>G. Wolf, Phys. Rev. **182**, 1538 (1969); and (private communication).

<sup>7</sup>Part of the  $\omega$  results presented in this paper include data from an earlier run for which the tagging range was slightly lower, 7.3 to 8.9 GeV.

<sup>8</sup>The OPE model also correctly describes  $\gamma p \rightarrow \omega p$  (unnatural-parity exchange) and  $\gamma p \rightarrow \omega \Delta$ . We have investigated the sensitivity of the OPE model to its vertex corrections by turning these corrections off. In this case, the mass distribution is proportional to the  $\pi^0 N$  total cross section (with the  $\Delta$  contribution removed). Using such a shape in the unfolding proce-

dure, we obtain  $\gamma N \rightarrow \omega \Delta$  cross sections 15% higher than given by unfolding with the full OPE model. As the vertex corrections used are certainly better than no corrections at all, this exercise suggests that the  $\gamma N \rightarrow \omega \Delta$  cross sections obtained have a model dependence less than  $\pm 15\%$ .

<sup>9</sup>Work of Y. Eisenberg *et al.*, as reported by A. Silverman, in *Proceedings of the 1975 International Symposium on Lepton and Photon Interactions at High Energies, Stanford, California*, edited by W. T. Kirk (SLAC, Stanford, 1976).

<sup>10</sup>G. Wolf, Nucl. Phys. **B26**, 317 (1971).

<sup>11</sup>The  $\gamma \pi \rho$  coupling strength has been taken from a  $\rho^0 \rightarrow \pi^0 \gamma$  radiative width of 100 keV obtained by scaling the  $\omega \rightarrow \pi^0 \gamma$  width by the factor 9, the simple SU(3) expectation. Had we instead used 35 keV as measured by Gobbi *et al.* [Phys. Rev. Lett. **33**, 1450 (1974)], the calculated cross sections would have been a factor of 3 smaller.

<sup>12</sup>A. Donnachie *et al.*, Phys. Lett. **26B**, 161 (1968). A compilation of  $\pi N$  partial-wave amplitudes, from this analysis and others, was kindly provided by the Particle Data Group, Lawrence Radiation Laboratory, University of California, Berkeley, California.